Decoupling Control of Six-Pole Radial Active Magnetic Bearings Based on BP Neural Network Inverse Optimized by Improved Mind Evolutionary Algorithm

Zhihao Ma and Huangqiu Zhu

***Abstract*—To solve the coupling issues of radial displacements in the two degrees of freedom of a six-pole radial active magnetic bearing (AMB) rotor, a decoupling control strategy based on backpropagation neural network (BPNN) inverse optimized by an improved mind evolutionary algorithm (MEA) is proposed. First, the structure and working principle of the six-pole radial AMB are introduced, and its mathematical model is derived. Second, an inverse model is constructed using a BPNN. To solve the sensitivity to initial weights and thresholds effectively, the improved MEA is designed with an adaptive subpopulation size strategy and an adaptive variance adjustment strategy. Finally, simulation studies of the six-pole radial AMB system are performed, and experiments on rotor floating, antidisturbance, and decoupling performance are complemented. The results verify the effectiveness and reliability of the proposed control strategy.**

***Index Terms*—Active magnetic bearing (AMB), backpropagation neural network(BPNN), decoupling control, inverse system, mind evolutionary algorithm (MEA).**

I. Introduction

A MAGNETIC bearing uses magnetic forces to suspend the rotor in space, eliminating mechanical contact between the rotor and stator. This design eliminates the need for lubrication and seals, fundamentally transforming the conventional bearing support structure [1], [2], [3], [4]. Magnetic bearings are widely applied in applications such as high-speed motors, compressors, marine rotating equipment, and flywheel energy storage [5], [6]. In active magnetic bearings (AMBs), the bias magnetic flux is generated by coil excitation and the suspension force by electromagnetic action, offering structural simplicity and precise control. This configuration is applied to a 16-pole AMB with tuned positive position feedback control in [7], and its whirling motion and rub/impact phenomena are examined in [8], highlighting the applicability of AMBs in complex dynamic environments. Conventional radial magnetic bearings typically employ four or eight magnetic poles to realize radial suspension control with two degrees of freedom, necessitating four unipolar or two bipolar switching power amplifiers for actuation [9], [10]. However, the significant drawbacks of these power amplifiers, namely their large volume and high cost, impose considerable constraints on the widespread application of magnetic bearings [11], [12]. Inverter-driven magnetic bearings require only a three-phase power inverter to achieve suspension in two radial degrees of freedom, thereby reducing the overall size and cost of the system [13]. The three-phase inverter technology is well-established in motor applications, and the same modern control techniques used in motor systems can be adapted to inverter-driven magnetic bearings. This enables the straightforward use of motor-related theories and digital control strategies, reducing the research and development costs of inverter-driven magnetic bearings. Therefore, inverter-driven magnetic bearings demonstrate significant potential in scenarios requiring high precision and low cost. Due to the asymmetry of the stator magnetic circuit, conventional three-pole AMBs exhibit pronounced nonlinearity between the control current and the suspension force. The six-pole AMB stator is designed with a symmetrical six-pole structure. This symmetry is a key feature aimed at simplifying the control problem by reducing system nonlinearity and coupling, which is critical for achieving stable operation [14]. This design provides a high load capacity per unit volume while maintaining a compact structural configuration. However, when the rotor is subjected to large external disturbances and deviates from its equilibrium position, the force-current characteristics in different directions remain strongly coupled, making precise control difficult. Therefore, decoupling control technology for six-pole AMBs holds significant research value.

Inverse system theory is a fundamental method for achieving decoupling control in complex systems. By compensating for the original system dynamics, it transforms the system into a pseudo-linear form with a linear transfer function, allowing the application of linear control techniques. However, its effectiveness relies on the accuracy of the inverse model, making

Received 21 April 2025; revised 11 August 2025; accepted 21 August 2025. Date of publication 26 August 2025; date of current version 13 November 2025. This work was supported in part by the National Natural Science Foundation of China under Grant 62273168 and in part by the Postgraduate Research & Practice Innovation Program of Jiangsu Province under Grant KYCX24_3972. Recommended for publication by Associate Editor R. Kennel. *(Corresponding author: Huangqiu Zhu.)*

The authors are with the School of Electrical and Information Engineering, Jiangsu University, Zhenjiang 212013, China (e-mail: 2112307119@stmail.ujs.edu.cn; zhuhuangqiu@ujs.edu.cn).

Color versions of one or more figures in this article are available at https://doi.org/10.1109/TPEL.2025.3602810.

Digital Object Identifier 10.1109/TPEL.2025.3602810

precise model construction a key challenge. In [15] and [16], the inverse system model is derived from the system's mathematical equations. However, for highly nonlinear or time-varying systems, this method often lacks accuracy due to the complexity of system dynamics, which are difficult to capture with simplified models. In [17], [18], and [19], the use of a least squares support vector machine (LSSVM) to approximate the inverse system model is proposed. Although LSSVM demonstrates its capability in handling nonlinear problems, its performance is highly dependent on the proper selection of the kernel function type, its associated parameters, and the regularization parameter. This parameter optimization process often lacks systematic theoretical guidance and can be computationally expensive. An improper selection can easily lead to model overfitting or underfitting, thereby reducing its generalization ability and ultimately compromising the effectiveness and overall performance of the control system.

Neural networks are widely used in constructing inverse system models due to their strong nonlinear mapping capabilities and the advantage of not requiring complex mathematical modeling. In [20], a traditional backpropagation neural network (BPNN) is employed to approximate the nonlinear inverse model of a bearingless permanent magnet synchronous motor. In [21], a general regression neural network (GRNN) is applied to model the inverse system of a vehicle chassis. Unlike BPNNs, GRNNs require only the tuning of a smoothing factor σ, without manual configuration of the network structure. Nevertheless, their performance in highly nonlinear and strongly coupled conditions remains limited. In [22], a fuzzy neural network (FNN) is utilized to build the inverse system model. While FNNs can effectively approximate nonlinear functions, their complex online inference process imposes a substantial computational burden, which is a major bottleneck for systems with stringent real-time requirements like high-speed AMBs.

The mind evolutionary algorithm (MEA) is an effective global optimization algorithm. Due to its advantages in overcoming the tendency of traditional optimization methods to fall into local optima, it is often used to optimize the parameters of complex models like neural networks. In [23], MEA is utilized to optimize the initial weights and thresholds of a multilayer perceptron (MLP) neural network for wind speed forecasting. In [24], MEA is applied to globally search for the optimal parameters of a wavelet neural network for short-term traffic flow prediction. While both studies demonstrate the effectiveness of MEA, the traditional MEA framework has inherent limitations. The fixed subpopulation size and search strategy of the algorithm lead to inefficient resource allocation and struggle to balance global exploration with local exploitation, making it prone to premature convergence when optimizing complex inverse system models.

In this article, a BPNN optimized by an improved mind evolutionary algorithm (IMEA) is proposed to achieve decoupling control of a six-pole radial AMB. An improved MEA is proposed to solve the issues of slow convergence and susceptibility to local optima in the process of inverse system modeling. By introducing an adaptive subpopulation size strategy and an adaptive variance strategy, the algorithm significantly enhances search efficiency and global optimization capability. The trained inverse model is connected in series with the original system to form a pseudo-linear system, thereby achieving system decoupling control. Simulation and experimental results demonstrate that the proposed method exhibits excellent decoupling performance and anti-interference capability.

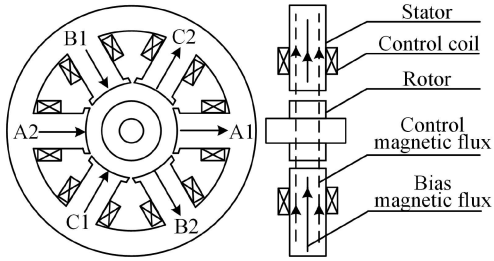

Fig. 1. Structure of six-pole radial active magnetic bearings.

II. Working Principle and Mathematical Model of a Six-Pole Radial AMB

A. Working Principle

As shown in Fig. 1, the structure of the six-pole radial AMB consists mainly of a rotor, a stator, and three-phase control coils. The stator comprises a yoke and six symmetrically distributed stator poles. Control coils are wound around each stator pole, with opposing poles connected in series in the same winding direction to form one phase. The three phases are star-connected and driven by a three-phase power inverter.

The six-pole radial AMB operates on the bearingless motor principle. The pole pair number of the torque coil P_{M} is 0, whereas the pole pair number of the suspension force coil P_{B} is 1. This configuration meets the requirement for generating radial suspension force [25]. Once the control coils are energized, the suspension force coil generates a rotating magnetic field with a pole pair number of 1. By adjusting the current, the magnetic field attraction of the six magnetic poles is changed to achieve the stable suspended equilibrium position of the rotor. When the rotor deviates from its equilibrium position, the displacement sensor detects the deviation and feeds the displacement signal back to the controller. The controller converts the displacement signal into a current signal. The output current signal is compared with the real-time current of the three-phase coils detected by the current sensors. By adjusting the switching devices of the three-phase inverter, the magnitude and direction of the current are controlled, changing the magnetic attraction of each pole and restoring the rotor to its equilibrium position.

B. Mathematical Model

To simplify the calculations, the influences of stator reluctance, magnetic saturation effects, leakage flux between poles, material losses, magnetic saturation phenomena, and eddy currents are neglected in the analysis.

The equivalent magnetic circuit of the six-pole radial AMB is shown in Fig. 2. Φ_{A1}, Φ_{A2}, Φ_{B1}, Φ_{B2}, Φ_{C1}, and Φ_{C2} represent the magnetic fluxes in the radial air gap. N is the number of turns

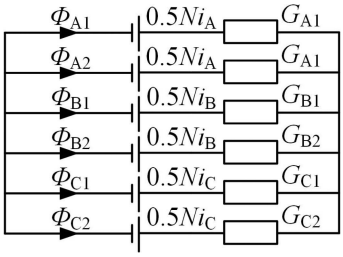

Fig. 2. Equivalent magnetic circuit.

in the radial coils and i_A, i_B, and i_C are the control currents. G_{A1}, G_{A2}, G_{B1}, G_{B2}, G_{C1}, and G_{C2} are the magnetic permeability of the radial air gap.

The expressions are given as follows:

$$\begin{cases} G_{A1} = \mu_0 S_r/(\delta_r - x) \\ G_{A2} = \mu_0 S_r/(\delta_r + x) \\ G_{B1} = \mu_0 S_r/\left(\delta_r + \frac{1}{2}x - \frac{\sqrt{3}}{2}y\right) \\ G_{B2} = \mu_0 S_r/\left(\delta_r - \frac{1}{2}x + \frac{\sqrt{3}}{2}y\right) \\ G_{C1} = \mu_0 S_r/\left(\delta_r + \frac{1}{2}x + \frac{\sqrt{3}}{2}y\right) \\ G_{C2} = \mu_0 S_r/\left(\delta_r - \frac{1}{2}x - \frac{\sqrt{3}}{2}y\right) \end{cases} \tag{1}$$

where δ_r is the radial air gap length when the rotor is at the equilibrium position, μ_0 is the vacuum permeability, the value is $4\pi\times10^{-7}$. S_r is the pole area, and x and y are radial displacements of the rotor.

According to Kirchhoff's law, the expressions for the magnetic fluxes are given as follows:

$$\begin{cases} \Phi_{A1} = \frac{1}{2}N\frac{G_{A1}}{G_{sum}}\left[(G_B + G_C)i_A - G_B i_B - G_C i_C\right] \\ \Phi_{A2} = \frac{1}{2}N\frac{G_{A2}}{G_{sum}}\left[(G_B + G_C)i_A - G_B i_B - G_C i_C\right] \\ \Phi_{B1} = \frac{1}{2}N\frac{G_{B1}}{G_{sum}}\left[(G_A + G_C)i_B - G_A i_A - G_C i_C\right] \\ \Phi_{B2} = \frac{1}{2}N\frac{G_{B2}}{G_{sum}}\left[(G_A + G_C)i_B - G_A i_A - G_C i_C\right] \\ \Phi_{C1} = \frac{1}{2}N\frac{G_{C1}}{G_{sum}}\left[(G_A + G_B)i_C - G_A i_A - G_B i_B\right] \\ \Phi_{C2} = \frac{1}{2}N\frac{G_{C2}}{G_{sum}}\left[(G_A + G_B)i_C - G_A i_A - G_B i_B\right] \end{cases} \tag{2}$$

where $G_{sum} = G_{A1}+G_{A2}+G_{B1}+G_{B2}+G_{C1}+G_{C2}$, $G_A = G_{A1}+G_{A2}$, $G_B = G_{B1}+G_{B2}$, and $G_C = G_{C1}+G_{C2}$.

Based on the relationship between the air gap flux and the electromagnetic force, the radial suspension force of each phase can be expressed as follows:

$$\begin{cases} F_A = \left(\frac{\Phi_{A1}^2}{2\mu_0 S_r} - \frac{\Phi_{A2}^2}{2\mu_0 S_r}\right) \\ F_B = \left(\frac{\Phi_{B1}^2}{2\mu_0 S_r} - \frac{\Phi_{B2}^2}{2\mu_0 S_r}\right) \\ F_C = \left(\frac{\Phi_{C1}^2}{2\mu_0 S_r} - \frac{\Phi_{C2}^2}{2\mu_0 S_r}\right) \end{cases}. \tag{3}$$

Assuming the initial condition that the rotor is at its equilibrium position and all radial air gap lengths are equal, $G_{A1} = G_{A2} = G_{B1} = G_{B2} = G_{C1} = G_{C2}$. (3) is expanded in a Taylor series around the equilibrium position, neglecting second-order and higher-order infinitesimal terms. By projecting the suspension forces onto the x and y directions, the following expressions are obtained:

$$\begin{cases} F_x = F_{1x} + F_{2x} = k_i \cdot i_x + k_l \cdot x \\ \quad = \frac{\sqrt{3}}{\sqrt{2}} \cdot \frac{5S_r\mu_0 N^2 I}{24\delta_r^2} \cdot i_x + \frac{5S_r\mu_0 N^2 I^2}{24\delta_r^3} \cdot x \\ F_y = F_{1y} + F_{2y} = k_i \cdot i_y + k_l \cdot y \\ \quad = \frac{\sqrt{3}}{\sqrt{2}} \cdot \frac{5S_r\mu_0 N^2 I}{24\delta_r^2} \cdot i_y + \frac{5S_r\mu_0 N^2 I^2}{24\delta_r^3} \cdot y \end{cases} \tag{4}$$

$$\begin{bmatrix} i_x \\ i_y \end{bmatrix} = \begin{bmatrix} 1 & -\frac{1}{2} & -\frac{1}{2} \\ 0 & -\frac{\sqrt{3}}{2} & \frac{\sqrt{3}}{2} \end{bmatrix} \begin{bmatrix} i_A \\ i_B \\ i_C \end{bmatrix} \tag{5}$$

where $k_i = \frac{\sqrt{3}}{\sqrt{2}} \cdot \frac{5S_r\mu_0 N^2 I}{24\delta_r^2}$ and $k_l = \frac{5S_r\mu_0 N^2 I^2}{24\delta_r^3}$. k_i is the displacement stiffness coefficient and k_l is the current stiffness coefficient.

Based on rotor dynamics theory, the equation of motion for the six-pole radial AMB can be expressed as

$$\begin{cases} m\ddot{x} = F_x \\ m\ddot{y} = F_y \\ J_x\ddot{\theta}_x = -l_a F_y - J_z\Omega\dot{\theta}_y \\ J_y\ddot{\theta}_y = l_a F_x + J_z\Omega\dot{\theta}_x \end{cases} \tag{6}$$

where J_x, J_y, and J_z are the moments of inertia around the x, y, and z axes. $J_x = J_y = J_z = J_d$, where J_d is the radial moment of inertia. l_a is the distance from the center of mass to the position of the magnetic bearing. l_b is the straight-line distance between the auxiliary bearing and the rotor's center of mass. θ_x and θ_y are the rotation angles of the rotor around the x and y axes. Ω is the mechanical angular velocity.

The state equation is

$$\begin{cases} \ddot{x} = \frac{k_x}{m}(1 + \frac{ml_a^2}{J_d})x + \frac{k_{ix}}{m}(1 + \frac{ml_a^2}{J_d})i_x - \frac{J_z\Omega}{J_d}\dot{y} \\ \ddot{y} = \frac{k_y}{m}(1 + \frac{ml_a^2}{J_d})y + \frac{k_{iy}}{m}(1 + \frac{ml_a^2}{J_d})i_y + \frac{J_z\Omega}{J_d}\dot{x} \end{cases}. \tag{7}$$

C. Analysis of System Reversibility

Based on the mathematical model of the six-pole radial AMB, the establishment of the inverse system requires the selection of appropriate state, input, and output variables. The following definitions are used for the state variable $\boldsymbol{X}$, input $\boldsymbol{U}$, and output variable $\boldsymbol{Y}$:

$$\begin{cases} \boldsymbol{X} = [x_1, x_2, x_3, x_4]^T = [x, y, \dot{x}, \dot{y}]^T \\ \mathbf{U} = [u_1, u_2]^T = [i_x, i_y]^T \\ \mathbf{Y} = [y_1, y_2] = [x, y]^T \end{cases}. \tag{8}$$

Based on (6) and (7), the second-order state equations of AMB can be obtained

$$\begin{cases} \dot{y}_1 = \dot{x}_1 = x_3 \\ \ddot{y}_2 = \ddot{x}_2 = x_4 \\ \dot{x}_3 = \frac{k_x}{m}\left(1 + \frac{ml_a^2}{J_d}\right)x_1 + \frac{k_{ix}}{m}\left(1 + \frac{ml_a^2}{J_d}\right)u_1 \\ -\frac{J_z\Omega l_a}{J_d(l_a+l_b)}x_4 \\ \dot{x}_4 = \frac{k_y}{m}\left(1 + \frac{ml_a^2}{J_d}\right)x_2 + \frac{k_{iy}}{m}\left(1 + \frac{ml_a^2}{J_d}\right)u_2. \\ -\frac{J_z\Omega l_a}{J_d(l_a+l_b)}x_3 \end{cases} \tag{9}$$

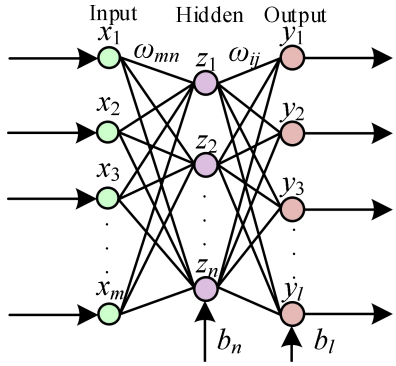

Fig. 3. Diagram of neural network structure.

According to the Interactor algorithm, the system's reversibility is analyzed by calculating the derivative of the output variable $\boldsymbol{Y}$ with respect to the input variable, continuing until the input variable $\boldsymbol{U}$ is included. The Jacobian matrix is presented as follows:

$$\begin{aligned}\mathbf{A} &= \left[\frac{\partial(\ddot{y}_1,\ddot{y}_2)}{\partial u}\right] = \begin{bmatrix}\frac{\partial \ddot{y}_1}{\partial u_1} & \frac{\partial \ddot{y}_1}{\partial u_2}\\ \frac{\partial \ddot{y}_2}{\partial u_1} & \frac{\partial \ddot{y}_2}{\partial u_2}\end{bmatrix}\\ &= \begin{bmatrix}\frac{k_{ix}}{m}\left(1+\frac{ml_a^2}{J_d}\right) & 0\\ 0 & \frac{k_{iy}}{m}\left(1+\frac{ml_a^2}{J_d}\right)\end{bmatrix}.\end{aligned} \tag{10}$$

From the above equation, it is determined that Rank($\boldsymbol{A}$) = 2. Since $\boldsymbol{A}$ is a full-rank 2×2 matrix and its determinant is nonzero, ensuring the matrix is invertible. The system exhibits a relative order of $\alpha = (\alpha_1,\alpha_2) = (2,2)$, giving a total relative order of 4 that equals the system order. These results demonstrate that the system is input–output invertible. The inverse system expression can be represented as follows:

$$[u_1,u_2]^{\mathrm{T}} = \varphi\left(y_1,\dot{y}_1,\ddot{y}_1,y_2,\dot{y}_2,\ddot{y}_2\right). \tag{11}$$

III. Establishment of the IMEA-BPNN Inverse System

A. Construction of the BP Neural Network

To accurately construct the inverse system model of a six-pole AMB, the IMEA-BPNN is proposed for this purpose. Due to its excellent nonlinear approximation capabilities and rapid convergence speed, the BPNN is widely employed for nonlinear system modeling. As shown in Fig. 3, the BP neural network consists of an input layer, a hidden layer, and an output layer. The input layer contains m neurons corresponding to the system's input dimensions, the output layer includes l neurons representing the system's output dimensions, and the hidden layer has n neurons, determined through empirical formulas or optimization algorithms. x_m represents the input of the mth neuron, z_{n} denotes the nth hidden layer node, y_l indicates the lth output layer node, ω_{mn} signifies the connection weight between x_m and z_n, ω_{nl} indicates the connection weight between z_n and y_l, b_n and b_l are the thresholds for the hidden layer and output layer, respectively.

The inverse system of AMB has six inputs and two outputs. Therefore, the number of nodes in the input layer and output layer is set to 6 and 2, respectively. Based on experience, the number of hidden layers is set to 10. Thus, the maximum values of the three parameters m, n, and l are 6, 10, and 2 in sequence.

The input layer is responsible for receiving input data and transmitting the input vector to the hidden layer for preprocessing. The output of the input layer nodes can be expressed as

$$v_m^1(k) = x_m, m = 1,2,\ldots,6 \tag{12}$$

where x_m is the input variable, and v_m^1 is the output of the input layer, the superscripts 1, 2, and 3 represent the input layer, hidden layer, and output layer, respectively.

The input and output of each node of the hidden layer can be expressed as

$$\begin{cases}u_n^2(k) = \sum_{m=1}^{6}\left[\omega_{mn}v_m^1(k)\right] - b_n(k)\\ v_n^2(k) = f(u_n^2(k))\end{cases} n = 1,2,\ldots,10 \tag{13}$$

where ω_{ij} is the weights of the hidden layer, b_j is the threshold of the hidden layer neurons, and $f(x)$ is the activation function.

The hidden layer employs the hyperbolic tangent function as the activation function for the nodes, which can be expressed as

$$f(x) = \frac{e^x - e^{-x}}{e^x + e^{-x}}. \tag{14}$$

The input and output expressions for the output layer are as follows:

$$\begin{cases}u_l^3(k) = \sum_{n=1}^{10}\left[\omega_{nl}v_j^2(k)\right] - b_l(k)\\ v_l^3(k) = g(u_l^3(k))\end{cases} l = 1,2. \tag{15}$$

The output layer employs the sigmoid function as the activation function for the nodes, which can be expressed as

$$g(x) = \frac{1}{1+e^{-x}}. \tag{16}$$

The objective of training the BP neural network is to minimize the mean square error between the network output and the expected output. After the kth iteration, the total error metric of the network is expressed as

$$E(k) = \frac{1}{2}\sum_{i=1}^{p}\left(Y_i(k) - \hat{Y}_i(k)\right)^2 = \frac{1}{2}\sum_{i=1}^{p}\left[e_i(k)\right]^2 \tag{17}$$

where Y_{i} is the actual network output, $\hat{Y}_i$ is the expected network output, p is the total number of training samples, and $e_{\mathrm{i}}(k)$ represents the error.

The BP neural network commonly employs gradient descent to adjust its weights. This method initially focuses on modifying the weights ω_{nl} between the hidden layer and the output layer. The weight ω_{nl} is adjusted in the direction of the negative gradient, and the adjustment amount for the weight is

$$\Delta\omega_{nl}(k) = -\eta\frac{\partial E(k)}{\partial\omega_{nl}(k)} \tag{18}$$

where η is the learning rate between the input layer and hidden layer, which is used to adjust the magnitude of the weight correction. The learning rate is set to 0.1.

The updated weight is

$$w_{nl}(k+1) = w_{nl}(k) + \Delta w_{nl}(k). \tag{19}$$

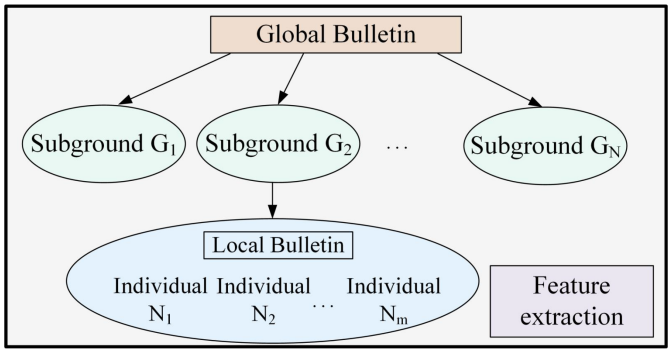

Fig. 4. Diagram of MEA system structure.

The adjustment of the weights $\omega_{mn}(k)$ between the input layer and the hidden layer follows the same procedure as in (19). The adjustment amount for the weight ω_{mn} is

$$\Delta\omega_{mn}(k) = -\gamma\frac{\partial E(k)}{\partial\omega_{mn}(k)} \tag{20}$$

where γ is the learning rate between the input layer and hidden layer, which is used to adjust the magnitude of the weight correction. The learning rate is set to 0.1.

The adjusted weight between the input layer and the hidden layer $\omega_{\mathrm{mn}}(k{+}1)$ is

$$\omega_{mn}(k+1) = \omega_{mn}(k) + \Delta\omega_{mn}(k). \tag{21}$$

During the training process, the weights are gradually optimized through multiple iterations, continuously improving the network's predictive performance.

B. Improved MEA

1) Traditional MEA: The BPNN optimizes the weights and thresholds through iterative training to gradually reduce the error between predicted and target outputs. The selection of initial weights and thresholds significantly influences the convergence speed and accuracy of the BP neural network. To mitigate the challenges arising from this selection, the MEA is integrated with the BPNN to optimize its network parameters, employing global search strategies to avoid local optima and thereby enhancing both convergence speed and accuracy. The MEA, an evolutionary algorithm inspired by principles of mutation and natural selection, exhibits robust global optimization and parallel processing capabilities, making it well-suited for this task. This combined MEA-BPNN approach significantly improves the precision and efficiency of inverse system modeling for six-pole AMBs, paving the way for more effective decoupling control in high-precision applications.

The structural framework of the system is shown in Fig. 4.

The MEA operates within an environment consisting of a bulletin board and multiple subpopulations. A key step in the algorithm involves selecting individuals based on their fitness scores, identifying the best performers along with some temporarily selected individuals. The selected individuals form new subpopulations, consisting of winning and temporary subpopulations. The algorithm applies convergence and diversification operations to these subpopulations. The detailed steps of the MEA are outlined as follows.

1) *Initial evaluation:* A population of size *T* is randomly generated within the solution space. Each individual is evaluated based on the fitness function. The results are sorted, and *M* high-scoring individuals (winning individuals) and *N* lower-scoring individuals (temporary individuals) are selected. The fitness function is defined as follows:

$$\text{Fitness} = \frac{1}{\frac{1}{N_{\mathrm{t}}}\sum_{k=1}^{p}\left(T_k - O_k\right)^2} \tag{22}$$

where T_{k} is the actual output value of the network, O_{K} is the expected output value, and *p* is the number of training data.

2) *Division of initial subpopulations:* Each of the *M* winning individuals and *N* temporary individuals serves as a center point. Around each center point, new individuals are generated following a normal distribution, where the center point acts as the mean, and a defined radius determines the standard deviation σ. These individuals form *M* winning subpopulations and *N* temporary subpopulations. To avoid overlap and duplication, the radius is carefully chosen to ensure separation between subpopulations.
3) *Subpopulation convergence operation:* In each subpopulation, individuals compete with each other, and the individuals with the highest fitness values are selected as winners. Further searches are then conducted around these winners according to a normal distribution until no new individual obtains a higher fitness value. At this point, the convergence operation of the subpopulations ends.
4) *Subpopulation diversification operation:* Winning subpopulations and temporary subpopulations compete against each other. If a temporary subpopulation achieves a higher overall fitness score compared to the winning subpopulation, the winning subpopulation is replaced by the temporary subpopulation. All individuals in the replaced subpopulation are discarded and redistributed within the solution space.
5) *Optimal solution determination:* Steps (3) and (4) are repeated until a stopping condition is met. The stopping condition can either be reaching the maximum number of iterations or achieving a sufficiently good fitness value. Once this condition is met, the algorithm terminates, and the individual with the highest fitness score is identified as the optimal solution.

2) Improved MEA:

a) Adaptive subpopulation size strategy: The traditional MEA generates subpopulations based on the principles of centering around winning and temporary individuals. According to the normal distribution, a fixed number of individuals are generated, leading to winning subpopulations and temporary subpopulations of the same scale. Nevertheless, winning individuals have a higher probability of survival. In contrast to temporary individuals, they can produce more offspring closer to

the optimal values. Consequently, more individuals are dispersed around winning individuals, causing the size of the winning subpopulation to be larger. To solve this issue, the MEA is enhanced by dynamically adjusting the number of individuals around each subpopulation based on their scores. As evolution progresses, more resources are allocated to winning individuals, enabling faster convergence towards optimal solutions while maintaining population diversity.

To implement the principles described above, the IMEA algorithm proceeds through a series of well-defined steps. These steps include evaluating individual scores and adjusting the number of generated individuals. The following sections outline these steps in detail:

1) *Score evaluation and classification:* The scores of individuals within the population are calculated and sorted, resulting in winning individuals x_0, x_1, …, $x_{\text{M-1}}$ and temporary individuals x_{M}, $x_{\text{M+1}}$, …, $x_{\text{M+N-1}}$.
2) *Dynamic individual generation:* The score of individual x_{i} is f_{i}. Centered around x_{i}, individuals are generated according to a normal distribution, with the number of individuals represented as T_{i}. The expression for T_{i} is

$$T_i = \text{ceil}\left(\frac{e^{f_i}}{\sum_{i=0}^{M+N-1} e^{f_i}} T\right), i = 0, 1, \ldots, M+N-1 \tag{23}$$

where T denotes the total population size, ceil is the ceiling function, and the lower limit for T_{i} is set to 10.

b) Adaptive variance adjustment strategy: Subpopulations generate T_{i} individuals randomly within the search space according to an adaptive strategy based on their sizes and following a normal distribution. A large variance hinders precise searching, whereas a small variance may lead to the loss of optimal solutions. Therefore, fine searches are conducted around superior individuals, while extensive searches occur around temporary individuals, ensuring both search efficiency and diversity among individuals.

$f_{\max}$ represents the score of the optimal individual in the population and $f_{\min}$ signifies the lowest score among the temporary individuals. The adaptive relationship for the variance adjustment coefficient α is defined as

$$\alpha(f_i) = \alpha_{\min} + \left(1 - \frac{f_i - f_{\min}}{f_{\max} - f_{\min}}\right) \times (\alpha_{\max} - \alpha_{\min}) \tag{24}$$

where $\alpha_{\max}$ is the maximum value of the variance adjustment coefficient and $\alpha_{\min}$ is the minimum value of the variance adjustment coefficient. In this article, $\alpha_{\max}$ is set to 2 and $\alpha_{\min}$ is set to 0.

The next step variance is

$$\sigma_{k+1} = \alpha \sigma_k. \tag{25}$$

When the score of an individual is high, the variance is reduced, allowing for a focused search in the vicinity of superior individuals. Conversely, when the score of an individual is low, the variance increases, expanding the search range around temporary individuals. The principle of generating individuals consistently follows the rule that higher scores correspond to lower variance.

The IMEA introduces an adaptive subpopulation sizing strategy in which higher-fitness elite individuals are allocated larger sub-populations, allowing the algorithm to intensify the search in more promising regions and accelerate convergence toward the global optimum. In addition, it employs an adaptive variance adjustment strategy where smaller variances are applied to elites to perform fine-grained local searches and enhance optimization accuracy, whereas larger variances are assigned to lower-fitness nonelite individuals to encourage broad global exploration, maintain population diversity, and effectively avoid local optima. These mechanisms work together to intelligently balance exploration and exploitation at different stages of the algorithm, resulting in faster convergence and stronger global search capability compared with the conventional MEA.

C. Establishment of the IMEA-BPNN Inverse Model

Establishing a precise analytical model is a prerequisite for implementing model-based control strategies, yet this is extremely challenging for complex nonlinear systems such as AMBs. To circumvent the reliance on a precise mathematical model, this article adopts a data-driven approach, utilizing the powerful nonlinear mapping capabilities of a BP neural network to directly identify the inverse dynamic model of the system.

The advantage of this method is that the neural network learns directly from experimental data that contains all the true dynamics of the system, thereby constructing a high-fidelity inverse model whose accuracy is not limited by the simplified analytical model. The following will detail the process of establishing the inverse model based on IMEA-BPNN. As shown in Fig. 5, the specific steps for establishing the inverse system decoupling model of the six-pole AMBs using the MEA-BP neural network are as follows.

1) *Determine inputs and outputs:* For the six-pole radial AMB inverse system, the inputs consist of displacement and its first and second derivatives $\{x, \dot{x}, \ddot{x}, y, \dot{y}, \ddot{y}\}$, whereas the output is the control current $\{i_{\text{x}}, i_{\text{y}}\}$. Initial values for the neural network weights and thresholds are set.
2) *Data collection and preprocessing:* A total of 2000 sets of input and output sample data are collected and normalized. 1400 sets are selected as the training sample set, while the remaining 600 sets are used as the test sample set.
3) *Set network structure:* Set the input layer with six nodes, the hidden layer with ten nodes, and the output layer with two nodes.
4) *Generate initial population:* Set the population size popsize = 200. Based on the fitness function, determine the winning and temporary individuals from the score results. By combining an adaptive subpopulation size strategy, form subpopulations of different scales.
5) *Subpopulation convergence:* Within the subpopulations, convergence is achieved through an adaptive strategy based on population size.
6) *Dissimilation operation:* The replacement between the winning subpopulation and the temporary subpopulation

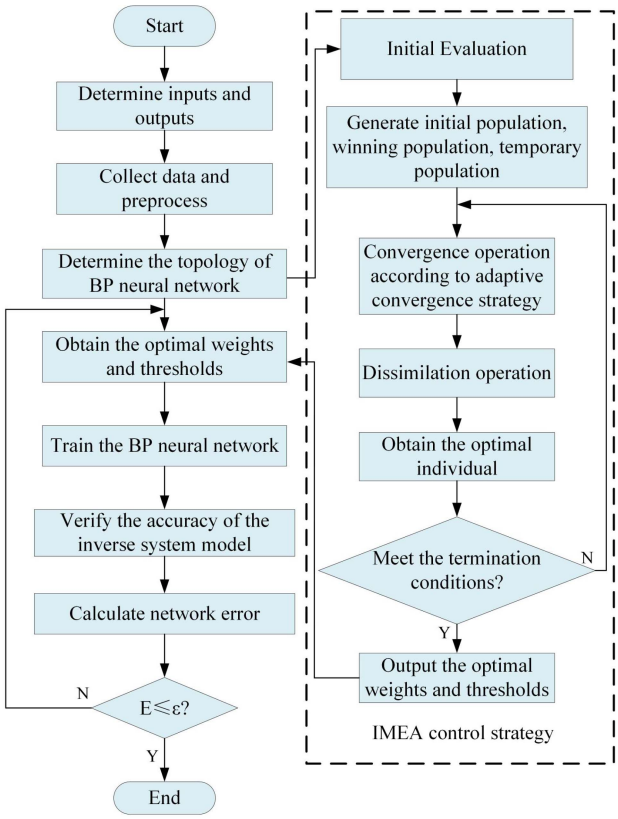

Fig. 5. Flowchart of IMEA-BPNN.

is completed, low-fitness subpopulations are eliminated, and new temporary subpopulations are generated.

7) *Iterate until convergence and output optimal individual:* Repeat steps 5 and 6 until the population score no longer increases, then the iteration ends and the optimal individual is output.
8) *Obtain optimal weights and thresholds:* The optimal values for the weights and thresholds of the BP neural network are extracted from the optimal individual.
9) *Train the BP neural network:* Use the training dataset to train the BP neural network, aiming to approximate the inverse system model.
10) *Validate the model:* The trained IMEA-BPNN inverse model is validated using the testing dataset.
11) *Performance evaluation and iterative optimization:* The performance metrics of the model are calculated. If the root mean square error is less than the preset accuracy ε, training is considered complete. If the training accuracy is not met, the process reverts to step (8) until the root mean square error is below the specified accuracy ε. ε is set to 1×10^{-4}.

A pseudo-linear system constructed based on the inverse system is an open-loop system that typically requires the design of a controller to achieve closed-loop control. The proportional-integral-derivative (PID) controller is a widely used control device in industrial production due to its simplicity and effectiveness. By integrating a PID controller into the pseudo-linear system, a composite control system based on the IMEA-BPNN algorithm is developed. The overall block diagram of the system is shown in Fig. 6.

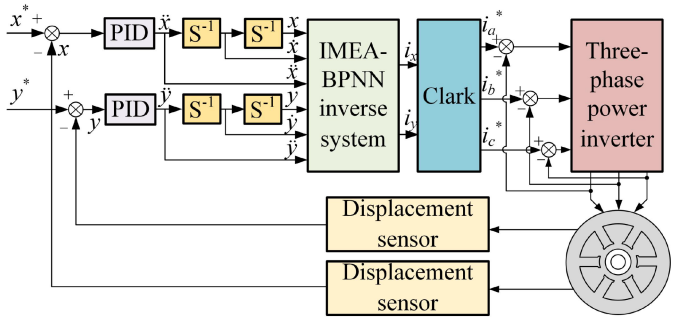

Fig. 6. Block diagram of six-pole radial AMB decoupling control based on IMEA-BPNN inverse.

The main computational burden of the proposed IMEA-BPNN control strategy is concentrated in the offline training phase. In this stage, significant computational resources are indeed required for the global optimization process of IMEA to obtain a high-precision inverse model. However, once the model is trained, the online real-time implementation only involves efficient feedforward network calculations, which imposes a minimal computational load and fully meets the stringent requirements of real-time control systems. This strategy of shifting the primary computational tasks to the offline design phase effectively trades for high performance and high efficiency in online control, demonstrating the feasibility and value of the method in engineering applications.

IV. Simulation Test

A. Collect Sample Data

The six-pole radial AMB adjusts the suspension force by varying the control current of the control coils, thereby ensuring stable rotor suspension. Consequently, the control currents (i_a, i_b, i_c) are selected as the input variables, whereas the rotor displacements (x, y) are the output variables.

Data are collected from the magnetic bearing system operating under a PID closed-loop controller. The output setpoint is a sinusoidal signal with varying frequencies, an amplitude of 0.5 mm, and a random disturbance of 0.1 mm. The sampling frequency is 10 000 Hz. Each sample duration is 0.1 ms, and the total runtime lasted 0.2 s. Stratified sampling extracts 2000 sets of real-time current and displacement data. Among these, 1400 sets are used for training, and 600 sets are used for testing the BP neural network. The finite difference method is applied to compute the displacement signal, along with its first and second derivatives. Normalized displacement data and their derivatives $\{x, \dot{x}, \ddot{x}, y, \dot{y}, \ddot{y}\}$ are utilized as inputs. Normalized control currents $\{i_x, i_y\}$ are employed as outputs.

B. Evaluation of the IMEA-BPNN Inverse Model

The IMEA is proposed to optimize the initial weights and thresholds of the BP neural network. To validate the effectiveness and superiority of the IMEA, this study compares

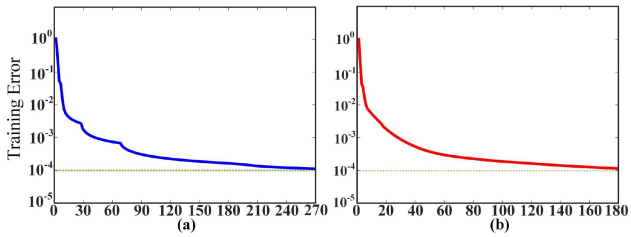

Fig. 7. Training error of (a) MEA-BPNN and (b) IMEA-BPNN.

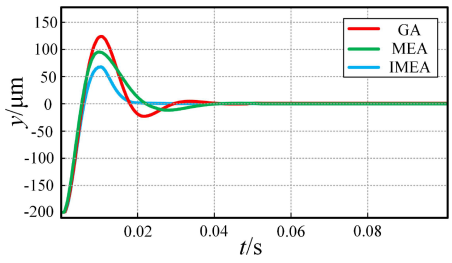

Fig. 8. Simulation waveforms of floating.

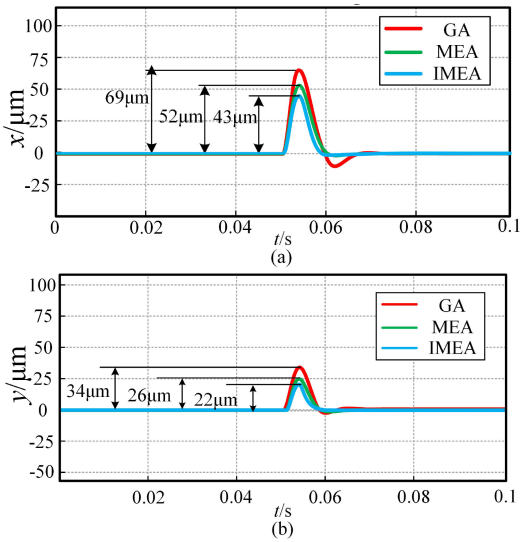

Fig. 9. Simulation waveforms in the (a) x direction and (b) y direction when the rotor is disturbed in the x direction.

the IMEA-BPNN with the traditional MEA-BPNN. The mean squared error (MSE) during training is used as the evaluation criterion. The training MSEs of the nonlinear inverse system models established by the MEA-BPNN and IMEA-BPNN are shown in Fig. 7. With a target training error set at 10^{-4}, the MEA-BPNN required 220 iterations to achieve the target accuracy, whereas the IMEA-BPNN reached the same within 170 steps. Furthermore, the IMEA-BPNN demonstrated excellent performance during training. The optimization algorithm effectively prevented the network from converging to local optima, significantly enhancing both training efficiency and effectiveness. This enables the IMEA-BPNN to achieve higher accuracy in less time, while also improving the model's stability and generalization capability.

C. Floating Simulation

To verify the effectiveness and superiority of the IMEA-BPNN, simulations of floating, decoupling, and antidisturbance abilities are conducted using MATLAB software.

Due to gravitational effects, the initial displacement of the six-pole radial AMB rotor is set to -200 μm in the y direction and 0 μm in the x direction. Simulations are conducted to evaluate the decoupling control performance of the inverse systems constructed with genetic algorithm (GA), MEA, and IMEA, with results shown in Fig. 8. By using the IMEA-BPNN decoupling control strategy, stable suspension is achieved in just 17 ms, whereas GA and MEA required 36 ms and 29 ms, respectively, to achieve suspension. Moreover, under the IMEA-BPNN, the rotor displacement exhibited the least overshoot, with faster response times, shorter rise times, and shorter peak times, demonstrating the most outstanding floating performance.

D. Step Disturbance Simulation

After the rotor achieves stable suspension at the equilibrium position, an external disturbance force of 50 N is applied in the x direction at 0.05 s. The rotor disturbance response displacement graphs based on three different decoupling control strategies are shown in Fig. 9. The displacement amplitudes in the x direction using the GA-BPNN and MEA-BPNN control strategies are 69 μm and 52 μm, respectively, whereas the x direction displacement amplitude for the IMEA-BPNN control strategy is 43 μm. The GA-BPNN and MEA-BPNN control strategies return to the equilibrium position after 30 ms and 24 ms, respectively, whereas the IMEA-BPNN strategy returns to equilibrium in just 12 ms. Additionally, due to the coupling relationship between the two degrees of freedom, a disturbance in the x direction also results in a displacement disturbance in the y direction. The displacement amplitudes in the y direction for the GA-BPNN and MEA-BPNN control strategies are 34μm and 26 μm, respectively, whereas the y direction displacement amplitude for the IMEA-BPNN inverse system control strategy is 22 μm. Simulation results indicate that when the AMB rotor is subjected to external disturbance forces, the IMEA-BPNN demonstrates superior disturbance rejection and decoupling capability compared to the other two control strategies.

V. Experimental Research

A. Experimental Platform

The main parameters of the six-pole radial AMB are given in Table I.

To validate the effectiveness of the proposed decoupling control strategy, a digital control test platform is established, as shown in Fig. 10. The platform primarily consists of the following components: a six-pole radial AMB, multiple displacement sensors, a displacement interface circuit board responsible for conditioning and converting sensor signals, a DSP, a drive power module, a simulator, and an ac/dc power supply. For the core controller, the TMS320F28335 from Texas Instruments is selected as the DSP minimal control system chip. This signal processing chip integrates extensive peripherals and bus functionalities,

TABLE I
MAIN PARAMETERS OF SIX-POLE RADIAL AMB

Parameters	Values
Radial air gap length δ_0	0.5 mm
Saturation induction density B_s	0.8 T
Magnetic pole area S_r	450 mm^2
Maximum ampere-turns of a radial coil ($N_r i_{rmax}$)	160 At
Outer diameter of rotor	32 mm
Inner diameter of rotor	16 mm
Axial length of rotor	35 mm
Rated radial load capacity	200 N

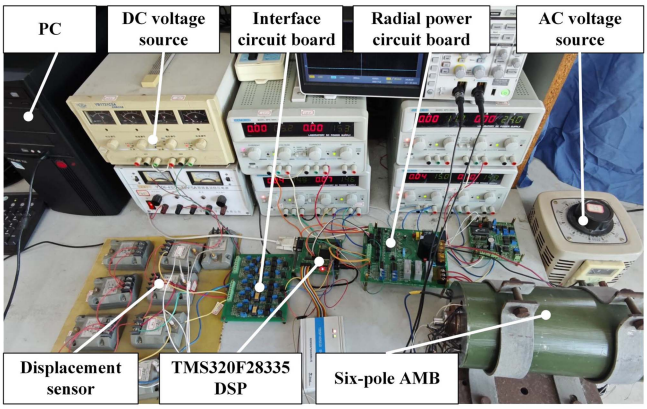

Fig. 10. Experiment platform.

making it highly suitable for various complex control application environments. Programming and development are performed using the integrated development environment Code Composer Studio. The displacements in the x and y directions are measured in a noncontact manner by four high-precision eddy-current displacement sensors (model OD-900803-03-07-20-00) mounted at orthogonal positions. These sensors offer micrometer-level resolution and a wide frequency response (dc-20 MHz), ensuring accurate and reliable displacement feedback during dynamic operation.

Additionally, to prevent damage from rotor-stator collision during system instability, auxiliary bearings are installed at both ends of the bearing assembly as a physical protection measure. Auxiliary bearings with a 0.2 mm clearance are installed at both ends of the rotor, serving as a standard physical protection measure. Their function is to prevent contact between the rotor and stator during unexpected operating conditions, such as system instability or power failure, thereby ensuring the safety of the experimental prototype. This platform allows for the systematic testing and evaluation of the dynamic response and robustness of the decoupling control strategy under different operating conditions.

B. Floating Experiment

In the de-energized state of the six-pole AMB, the rotor resides on its auxiliary bearings under the influence of its own weight. A comparison of rotor displacement waveforms upon energization, evaluating three decoupling control strategies:

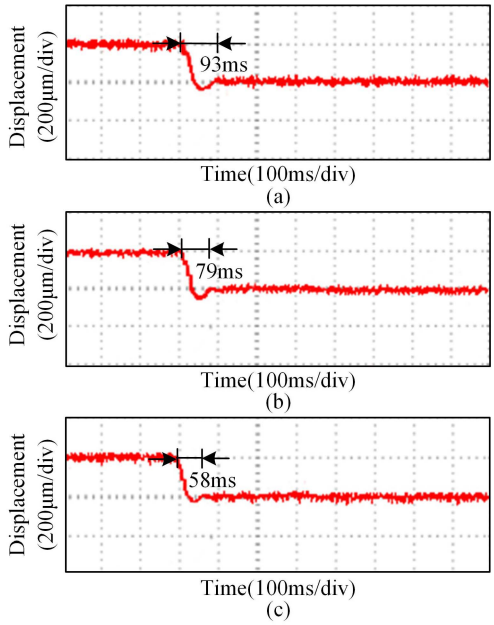

Fig. 11. Experiment results of floating under (a) GA-BPNN, (b) MEA-BPNN, and (c) IMEA-BPNN.

the conventional genetic-algorithm backpropagation neural network (GA-BPNN), MEA-BPNN, and IMEA-BPNN, is shown in Fig. 11. Distinct dynamic behaviors are observed for each strategy. The IMEA-BPNN approach achieves rotor stabilization at the equilibrium position in a significantly shorter time frame of 58 ms, compared to 93 ms for GA-BPNN and 79 ms for MEA-BPNN. These represent reductions in settling time of 37.6% and 26.6%, respectively. Moreover, the IMEA-BPNN control strategy results in a diminished overshoot in the displacement profile, indicating superior dynamic characteristics and control accuracy. These experimental results confirm the efficacy of the IMEA-BPNN control strategy.

C. Anti-Interference Experiment

When the rotor is in a stable suspension state, an external disturbance force of 80 N in the x direction is generated by hanging weights at one end. The rotor displacements under the external disturbance for three decoupling control strategies are shown in Fig. 12. Under the GA-BPNN and MEA-BPNN inverse system control strategies, the maximum rotor displacements are 138 μm and 98 μm, respectively, with recovery times of 203 ms and 194 ms back to the equilibrium position. In contrast, under the IMEA-BPNN control strategy, the maximum displacement is significantly reduced to 85 μm, representing a decrease of approximately 38.4% compared to GA-BPNN and 13.3% compared to MEA-BPNN. Additionally, the recovery time under IMEA-BPNN is shortened to 172 ms, about 15.3% and 11.3% faster compared with GA-BPNN and MEA-BPNN, respectively. These experimental results clearly indicate that the IMEA-BPNN inverse system demonstrates superior antidisturbance capability and faster response performance compared to both the GA-BPNN and MEA-BPNN inverse systems.

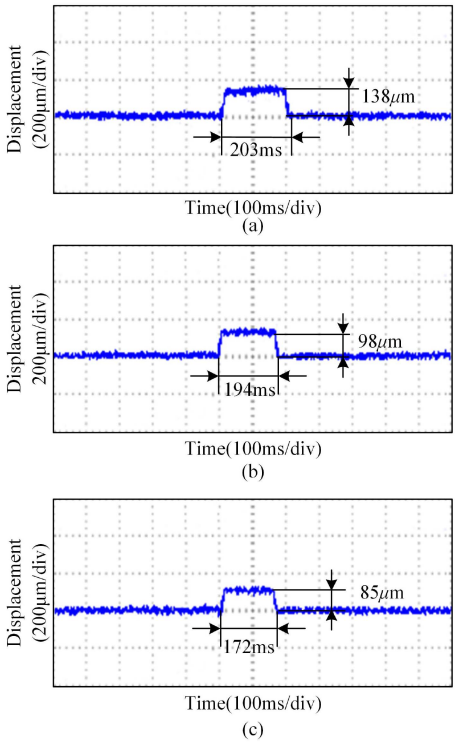

Fig. 12. Experiment results of anti-interference under (a) GA-BPNN, (b) MEA-BPNN, and (c) IMEA-BPNN.

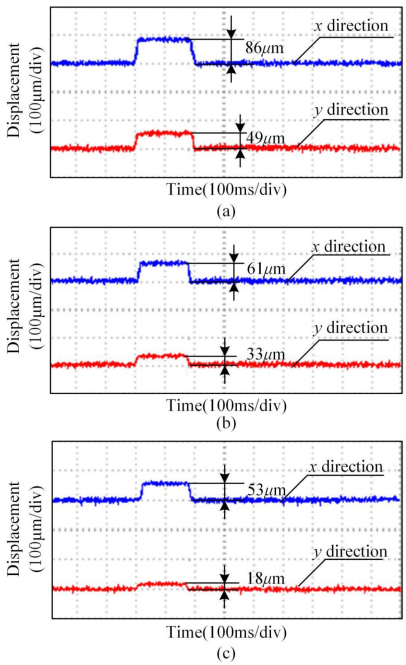

Fig. 13. Experiment results of decoupling under (a) GA-BPNN, (b) MEA-BPNN, and (c) IMEA-BPNN.

D. Decoupling Experiment

After the rotor deviates from the equilibrium position, coupling occurs in the x and y directions of the magnetic bearing. This coupling can lead to system instability and make precise control challenging [26], [27]. Such strategies significantly enhance system stability and control accuracy and reduce interference between directions. In the experiment, when the rotor is stably suspended at the equilibrium position, an external disturbance force of 50 N is applied in the x direction. The resulting coupling displacement in the y direction is measured. The experiment results of the decoupling performance on three control strategies are shown in Fig. 13. Under this disturbance, rotor displacements with GA-BPNN and MEA-BPNN inverse system control strategies are 86 μm and 61 μm in the x direction, and coupling displacements of 49 μm and 33 μm in the y direction, respectively. With the IMEA-BPNN inverse system, the rotor displacement is 53 μm in the x direction, representing reductions of 38.4% compared to GA-BPNN and 13.1% compared to MEA-BPNN. The coupling displacement in the y direction is 18 μm, which is 63.3% and 45.5% lower than that of GA-BPNN and MEA-BPNN, respectively. The experimental results clearly show that the IMEA-BPNN inverse system has superior decoupling performance, enhancing the precise control of AMBs.

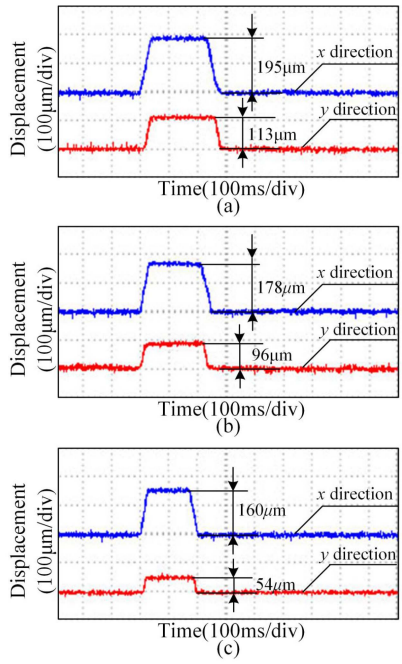

Fig. 14. Experimental results of decoupling performance under a 150 N step disturbance force for (a) GA-BPNN, (b) MEA-BPNN, and (c) IMEA-BPNN.

To evaluate decoupling performance under varying operating conditions, an external disturbance of 150 N is applied in the x direction, corresponding to 75% of the rated load capacity. The experimental results for the three control strategies are shown in Fig. 14. Under this disturbance, rotor displacements with GA-BPNN and MEA-BPNN control strategies are 195 μm and 178 μm in the x direction, and coupling displacements of 111 μm and 96 μm in the y direction, respectively. With the IMEA-BPNN, the rotor displacement is 160 μm in the x direction, representing reductions of 17.9% compared to GA-BPNN and

10.1% compared to MEA-BPNN. The coupling displacement in the y direction is 54 μm, which is 51.4% and 43.8% lower than that of GA-BPNN and MEA-BPNN, respectively. These experimental results fully demonstrate that the IMEA-BPNN control strategy maintains outstanding control precision and decoupling performance even under demanding conditions near the maximum load, providing the system with the largest safety margin and reliability.

VI. Conclusion

To solve the coupling issue of rotor displacements in the two radial degrees of freedom of the six-pole radial AMB system, a decoupling control strategy based on IMEA-BPNN inverse system is proposed. The simulation and experimental results demonstrate the effectiveness of the proposed decoupling control strategy. The following conclusions are obtained.

1) Based on the mathematical model and reversibility analysis of the six-pole AMB system, an inverse model of IMEA-BPNN is established. The results show that the six-pole AMB system is reversible and the proposed decoupling control method is feasible.
2) By introducing the adaptive subpopulation size strategy and the adaptive variance adjustment strategy, IMEA-BPNN solves the problem that MEA is easy to fall into a local optimum, optimizes the generation scale of the subpopulation, improves the search accuracy, and thus improves the global search ability, optimization accuracy, and efficiency of the algorithm.
3) The simulation and experimental results show that the decoupling control strategy of IMEA-BPNN inverse system significantly improves the response speed of six-pole radial AMB, effectively reduces the rotor displacement offset value caused by external interference and coupling effect, and has good anti-interference performance and decoupling ability.

References

[1] A. Chiba, T. Fukao, O. Ichikawa, M. Oshima, and M. Takemoto, *Magnetic Bearings and Bearingless Drives*. Amsterdam, The Netherlands: Elsevier, Mar. 2005.

[2] A. Kandil, L. Hou, M. Sharaf, and A. A. Arafa, "Configuration angle effect on the control process of an oscillatory rotor in 8-pole active magnetic bearings," *AIMS Math.*, vol. 9, no. 5, pp. 12928–12963, Apr. 2024.

[3] X. Li, A. Palazzolo, and Z. Wang, "A combination 5-DOF active magnetic bearing for energy storage flywheels," *IEEE Trans. Transp. Electrif.*, vol. 7, no. 4, pp. 2344–2355, Dec. 2021.

[4] N. A. Saeed, M. Eissa, and W. A. El-Ganini, "Nonlinear oscillations of rotor active magnetic bearings system," *Nonlinear Dyn.*, vol. 74, pp. 1–20, Jun. 2013.

[5] T. Pei, D. Li, J. Liu, J. Li, and W. Kong, "Review of bearingless synchronous motors: Principle and topology," *IEEE Trans. Transp. Electrif.*, vol. 8, no. 3, pp. 3489–3502, Sep. 2022.

[6] Z. Cui, Y. Zhou, and Y. Zhou, "Research on rotor radial position observation method of dual-winding bearingless flux-switching permanent magnet machines," *IEEE Trans. Ind. Electron.*, vol. 71, no. 4, pp. 6622–6634, Jul. 2024.

[7] A. Kandil and Y. S. Hamed, "Tuned positive position feedback control of an active magnetic bearings system with 16-poles and constant stiffness," *IEEE Access*, vol. 9, pp. 73857–73872, 2021.

[8] A. Kandil, "Investigation of the whirling motion and rub/impact occurrence in a 16-pole rotor active magnetic bearings system with constant stiffness," *Nonlinear Dyn.*, vol. 102, pp. 2247–2265, Nov. 2020.

[9] N. A. Saeed, E. M. Awwad, M. A. El-Meligy, and E. S. A. Nasr, "Radial versus cartesian control strategies to stabilize the nonlinear whirling motion of the six-pole rotor-AMBs," *IEEE Access*, vol. 8, pp. 138859–138883, 2020.

[10] A. Kandil, Y. S. Hamed, and A. M. Alsharif, "Rotor active magnetic bearings system control via a tuned nonlinear saturation oscillator," *IEEE Access*, vol. 9, pp. 133694–133709, 2021.

[11] C. Liu, J. Zhan, J. Wang, Y. Yang, and Z. Liu, "An improved one-cycle control algorithm for a five-phase six-leg switching power amplifier in active magnetic bearings," *IEEE Trans. Ind. Electron.*, vol. 69, no. 12, pp. 12564–12574, Dec. 2022.

[12] R. Yang, Z. Deng, C. Peng, and K. Li, "Frequency-varying suppression of vibration for active magnetic bearing using improved resonant controller," *IEEE Trans. Ind. Electron.*, vol. 69, no. 12, pp. 13494–13503, Dec. 2022.

[13] R. Schöb, C. Redemann, and T. Gempp, "Radial active magnetic bearing for operation with a 3-phase power converter," in *Proc. 4th. Int. Symp. Magn. Suspension Technol.*, Oct./Nov. 1997, pp. 111–124.

[14] N. A. Saeed, J. Awrejcewicz, A. Mousa, and M. S. Mohamed, "ALIPPF-Controller to stabilize the unstable motion and eliminate the non-linear oscillations of the rotor electro-magnetic suspension system," *Appl. Sci.*, vol. 12, no. 8, pp. 3902–3926, Apr. 2022.

[15] J. Fang and Y. Ren, "High-precision control for a single-gimbal magnetically suspended control moment gyro based on inverse system method," *IEEE Trans. Ind. Electron.*, vol. 58, no. 9, pp. 4331–4342, Sep. 2011.

[16] J. Wu and Y. Lu, "Decoupling and optimal control of multilevel buck DC–DC converters with inverse system theory," *IEEE Trans. Ind. Electron.*, vol. 67, no. 9, pp. 7861–7870, Sep. 2020.

[17] G. Liu, L. Chen, W. Zhao, Y. Jiang, and L. Qu, "Internal model control of permanent magnet synchronous motor using support vector machine generalized inverse," *IEEE Trans. Ind. Inform.*, vol. 9, no. 2, pp. 890–898, May 2013.

[18] W. Bu and Z. Li, "LS-SVM inverse system decoupling control strategy of a bearingless induction motor considering stator current dynamics," *IEEE Access*, vol. 7, pp. 132130–132139, 2019.

[19] B. Xu, H. Zhu, and X. Wang, "Decoupling control of outer rotor coreless bearingless permanent magnet synchronous motor based on least squares support vector machine generalized inverse optimized by improved genetic algorithm," *IEEE Trans. Ind. Electron.*, vol. 69, no. 12, pp. 12182–12190, Dec. 2022.

[20] X. Sun, L. Chen, H. Jiang, Z. Yang, J. Chen, and W. Zhang, "High-performance control for a bearingless permanent magnet synchronous motor using neural network inverse scheme plus internal model controllers," *IEEE Trans. Ind. Electron.*, vol. 63, no. 6, pp. 3479–3488, Jun. 2016.

[21] F. Xu, C. Zhou, X. Liu, and J. Wang, "GRNN inverse system based decoupling control strategy for active front steering and hydro-pneumatic suspension systems of emergency rescue vehicle," *Mech. Syst. Signal Process.*, vol. 167, pp. 4811–4822, Mar. 2022.

[22] C. Jiang, H. Zhu, and X. Wang, "Decoupling control of outer rotor coreless bearingless permanent magnet synchronous generator based on fuzzy neural network inverse system," *IEEE Trans. Transp. Electrif.*, vol. 9, no. 3, pp. 3908–3917, Sep. 2023.

[23] H. Liu, H. Tian, X. Liang, and Y. Li, "New wind speed forecasting approaches using fast ensemble empirical model decomposition, genetic algorithm, mind evolutionary algorithm and artificial neural networks," *Renewable Energy*, vol. 83, pp. 1066–1075, Jun. 2015.

[24] L. Xu, X. Du, and B. Wang, "Short-term traffic flow prediction model of wavelet neural network based on mind evolutionary algorithm," *Int. J. Pattern Recognit. Artif. Intell.*, vol. 32, no. 12, pp. 1850041–1850055, Jun. 2018.

[25] M. Wu, H. Zhu, H. Zhang, and W. Zhang, "Modeling and multilevel design optimization of an AC-DC three-degree-of-freedom hybrid magnetic bearing," *IEEE Trans. Ind. Electron.*, vol. 70, no. 1, pp. 233–242, Jan. 2023.

[26] N. A. Saeed, S. M. El-Shourbagy, M. Kamel, K. R. Raslan, and M. K. Aboudaif, "Nonlinear dynamics and static bifurcations control of the 12-pole magnetic bearings system utilizing the integral resonant control strategy," *J. Low Freq. Noise Vib. Act. Control*, vol. 41, no. 4, pp. 1532–1560, Jun. 2022.

[27] N. A. Saeed, M. S. Mohamed, S. K. Elagan, and J. Awrejcewicz, "Integral resonant controller to suppress the nonlinear oscillations of a two-degree-of-freedom rotor active magnetic bearing system," *Processes*, vol. 10, no. 2, Feb. 2022, Art. no. 271.

Zhihao Ma was born in Taizhou, China. He received the B.S. degree in electrical engineering from Chengxian College, Southeast University, Nanjing, China, in 2020. He is currently working toward the Ph.D. degree in electrical engineering with the School of Electrical and Information Engineering, Jiangsu University, Zhenjiang, China.

His research interests include optimal design and control of magnetic bearings.

Huangqiu Zhu was born in Taizhou, China. He received the B.S. and M.S. degrees in automation and management from Jiangsu University, Zhenjiang, China, in 1987 and 1993, respectively, and the Ph.D. degree in mechanical manufacture and automation from the Nanjing University of Aeronautics and Astronautics, Nanjing, China, in 2000.

He is currently with the School of Electrical and Information Engineering, Jiangsu University. His research interests include magnetic bearings, bearingless motors, and motor and movement control.